ISSN 1027-4510, Journal of Surface Investigation: X-ray, Synchrotron and Neutron Techniques, 2018, Vol. 12, No. 5, pp. 835–852. © Pleiades Publishing, Ltd., 2018.
Original Russian Text © E.V. Suvorov, 2018, published in Poverkhnost', 2018, No. 9, pp. 3–22.

X-Ray Topography: Yesterday, Today, and Prospects for the Future

E. V. Suvorov*

Institute of Solid State Physics, Russian Academy of Sciences, Chernogolovka, Moscow oblast, 142432 Russia

**e-mail: suvorov@issp.ac.ru*

Received December 28, 2017

Abstract—X-ray topography is a set of X-ray diffraction techniques that make it possible to see images of defects, to determine their type and location in the volume of the crystal structure or on its surface, and to measure their main characteristics. The review discusses the possibilities, limitations, and prospects of X-ray topography methods.

Keywords: X-ray diffraction microscopy, synchrotron radiation, Fujiwara method, Berg–Barrett method, Schulz method, Borrmann method, Lang method, quasi-planar waves

DOI: 10.1134/S1027451018050026

INTRODUCTION

X-ray topography (X-ray diffraction microscopy) is a group of X-ray diffraction methods that make it possible to see images of defects, and to determine their type and location in the volume of the crystal structure or on its surface.

Almost all of the most important properties of crystals are largely associated with crystal-lattice defects (this includes the electrical, optical, magnetic, and mechanical characteristics of the samples). For example, the electronic properties of semiconductors (electron and hole conductivity) are completely determined by impurity atoms, i.e., point defects of the crystal lattice. As is known, a pure semiconductor, for example silicon, is generally a dielectric. Another example is that the plasticity of materials is determined by the presence of a different type of defect, namely, dislocations. Therefore, for the practical use of crystals, it is very important to know their real structure, i.e., the presence of defects, their concentration, type, and location in the volume of the crystal lattice. For this purpose, many direct methods for studying the real structure of crystals have been developed, such as optical microscopy, transmission and scanning electron microscopy, X-ray topography, atomic force microscopy, tunneling microscopy, etc.

X-ray topography is of particular importance among direct methods, since it is a nondestructive method for controlling crystal lattices, which makes it possible to control the structure of large volumes of samples (with a width of up to about 10 mm and an area of up to about 10 cm^2) without damage and with little or no special surface preparation. It includes a whole range of methods. To understand how these methods work, it is necessary to recall some basic concepts of X-ray structural analysis. X-rays were discovered in 1894 by Roentgen (historically, he was the winner of the first Nobel Prize in Physics, 1901). In 1914, von Laue together with Knipping and Friedrich found that they are electromagnetic waves with a wavelength of about 1 Å = 10^{-10} m and, hence, can be diffracted at crystal lattices, the parameters of which are also approximately 1 Å. Von Laue developed the theory of X-ray scattering at a three-dimensional crystal lattice. At first, a kinematic theory that took into account only single scattering events was constructed, and then papers appeared that discussed a more complex dynamic theory involving multiple scattering.

The main conclusions of the kinematic theory can be understood from the analysis of Fig. 1. The pattern of X-ray scattering at a crystal is a set of individual spots of different brightness. These spots are not located randomly, but according to certain rules. The geometry of X-ray diffraction at a crystal lattice is described by the von Laue laws or by the more explicit Wulff–Bragg rule:

$$2d \sin \theta = \lambda. \quad (1)$$

Here d is the distance between the planes, at which diffraction takes place; θ is the diffraction angle (the Bragg angle, i.e., the half-angle between the directions of the incident and diffracted X-ray beams); and λ is the wavelength.

As follows from the von Laue theory, the coordinates of the diffraction spots in the X-ray diffraction pattern enable determination of the parameters of the unit cell of the crystal and its symmetry. Measurements of the intensity of diffraction spots make it possible to find the electron-density distribution in the unit cell, i.e., to determine the coordinates of all atoms. Finally, studying the fine structure of diffrac-

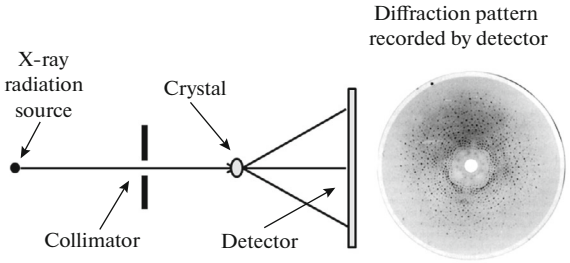

Fig. 1. Scheme of the X-ray experiment and a typical von Laue diffraction pattern.

tion spots and the structure of the diffuse background between reflections carries information about the real structure of the crystal, i.e., information about defects. Thus, studying the structure of diffraction spots allows one to gain information about the defects that are present in crystals.

PHYSICAL BASIS OF X-RAY TOPOGRAPHY

Back in the 1930s, a number of researchers noted that the plastic deformation of crystals causes an increase in the width of X-ray diffraction lines (the dependence of the intensity of the X-ray beam reflected from the crystal on the angle at the Bragg condition). Moreover, subsequent annealing processes can lead to the narrowing of diffraction lines and even to restoration of their original shape. It was also noted that there is a qualitative relationship between the mechanical, electrical, magnetic, and chemical characteristics of matter and diffraction-line shapes and the form of diffuse scattering. At the same time, semi-quantitative methods for analyzing the shape of diffraction lines were developed to determine the dimensions and alignment of blocks and microstresses that arise in the volume and at the interface of crystallites [1–3].

The idea of obtaining X-ray microdiffraction patterns (topograms) was proposed by Berg in 1931 [4, 5]. The physical meaning of his idea is clear from Fig. 2. If a divergent beam of X-rays is incident on a crystal, then waves of a certain length are reflected at each point of the crystal in accordance with the Wulff–Bragg law, i.e., a wave with a length of λ_1 is reflected at point *1*, a wave with a length of λ_2 at point *2*, and a wave with a length of λ_3 at point *3*. Let us assume that the intensities of these waves are practically the same (the divergence of the incident beam is small). If the crystal is perfect, i.e., the real structure of the crystal at points *1*, *2*, and *3* is the same, then the intensity of rays reflected at these points will be the same and, consequently, photographic film exposure at points *1*', *2*', and *3*' will also be the same. However, if there are any defects in the crystal structure at points *1*, *2*, and *3*, then their imaging reflections are seen in the topogram in the form of a change in the degree of black coloration. The fact is that the fields of local lattice microdeformations are always associated with defects; these regions deviate from the exact Bragg diffraction condition given by Eq. (1), so the intensities of rays *1*', *2*', and *3*' vary. This provides the diffraction image of the crystal in the X-ray topogram. It should be noted that the image of the crystal in the method proposed by Berg is transmitted one to one, i.e., without magnification. This applies to virtually all X-ray topography methods. For the subsequent detailed analysis of topograms, they must be magnified by optical methods.

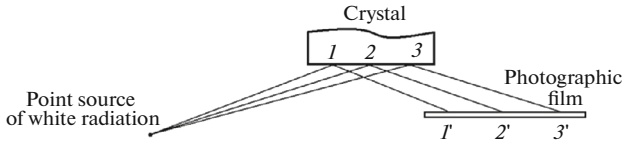

Fig. 2. Scheme of Berg's experiment.

The field of local deformations caused by defects consists of the following two components: the field of changes in the interplanar distances and the field of local misalignments of the crystal lattice. The total field of local deformations has been called the "combined distortion" in publications. In a simplified form, it is described by the formula,

$$\varepsilon(\mathbf{r}) = \frac{\Delta d}{d}\cot\theta + \Delta\theta. \qquad (2)$$

Here, $\mathbf{r}$ is the current radius vector of a point in the crystal volume.

It is easiest to understand the physical reasons for the formation of the diffraction image of crystal-lattice defects from the consideration of a hypothetical experiment. Let there be a crystalline sample, in ideal matrix *C* of which there are two islets *A* and *B* with parameters different from the matrix (Fig. 3a). Let us assume that the reflectivities of a selected system of planes (*hkl*) of the sample are R_A, R_B, and R_C, where $R_A > R_B$, and $R_B = R_C$. Let us also assume that n_A, n_B, and n_C are the normals to the reflecting system of planes, and the angles between the normals are $n_A \wedge n_C = 0$ and $n_B \wedge n_C = \alpha$, i.e., the angle between the normals to matrix *C* and islet *A* is zero, and the angle between the normals to matrix *C* and islet *B* is different from zero. The following two cases should be taken into consideration.

Let a polychromatic X-ray beam fall onto the sample, and let the spectral width $\Delta\lambda > 0$ be such that both the matrix and two islets are in the Bragg reflection position. Then both the matrix and two islets reflect X-ray radiation, and the image of the sample should appear in the X-ray topogram, with islet *A* being brighter and islet *B* being the same brightness as the matrix, i.e., islet *B* should not be visible against the background of the matrix *C* (Fig. 3b).

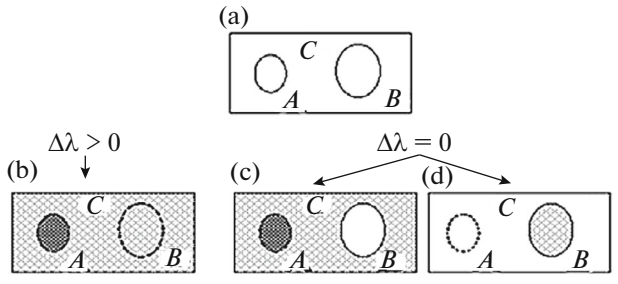

Fig. 3. Scheme explaining the mechanism of the formation of the diffraction contrast of defects.

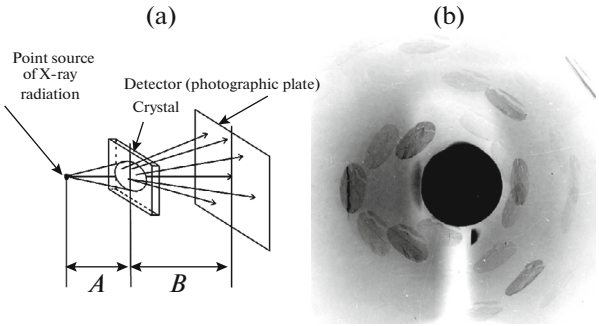

Fig. 4. (a) Scheme of the experiment proposed in [10] and (b) the X-ray diffraction pattern of a single LiF crystal when recorded according to this scheme at $A = 120$ mm, $B = 50$ mm, and a sample thickness of 0.3 mm by using the radiation of a Cu anode.

Let us consider the case when a monochromatic beam is incident on the crystal. Let us set the sample in the reflection position so that the Bragg condition is satisfied by matrix *C* and islet *A* (Fig. 3c). In accordance with the experimental conditions, islet *A* is shown brighter than the matrix, and islet *B* is excluded from the reflecting position and its image is a bright spot. If we rotate the sample by angle α so that islet *B* is in the reflection position, then matrix *C* and islet *A* are excluded from Bragg reflection, and the diffraction image corresponds to Fig. 3d, i.e., matrix *C* and islet *A* are not visible in the image. In general terms, this hypothetical experiment explains the mechanism of the formation of the diffraction image of defects in X-ray topograms.

Berg's idea was developed in subsequent studies by Berg, Barrett, Fujiwara, Newkirk, Schulz, Kohra, Bonse, Borrmann, Lang, and others [6–15]. A variety of X-ray optical schemes were proposed, which differed in terms of the linear and angular resolution, the degree of monochromatization of the used radiation, the focal-spot dimensions, and the divergence of the X-ray beam incident on the crystal. Let us discuss only some of the most common and frequently used topographic schemes.

In Russia and the former Soviet Union, interest in X-ray topography methods arose in the 1960s in connection with the study of the real structure of materials for solid-state electronics (silicon, germanium, and indium antimonide). The studies were carried out at almost the same time in many scientific centers, among which we should mention, first of all, the Ioffe St. Petersburg Physical-Technical Institute, Russian Academy of Sciences; Department of Physics, Moscow State University; Shubnikov Institute of Crystallography, Russian Academy of Sciences; Kurchatov Institute; Institute of Solid State Physics, Russian Academy of Sciences; Institute of Semiconductor Physics of Ukraine; Yerevan State University; and Yaroslav Mudryi Institute of Semiconductor Physics, Siberian Branch, Russian Academy of Sciences.

FUJIWARA METHOD

First, let us consider the Fujiwara scheme [9–11]. This method is interesting in that topograms of several different diffraction reflections are simultaneously obtained in the X-ray diffraction pattern, which allows one to determine the spatial arrangement of defects in the volume of the crystal (i.e., to construct tomograms). The X-ray optical scheme proposed by Fujiwara is shown in Fig. 4a, and a typical Fujiwara diffraction pattern is shown in Fig. 4b [10]. A divergent X-ray beam is directed to the crystal, and diffraction reflections similar to von Laue spots arise as a consequence. Each such spot is formed by reflection from a certain system of reflecting planes (*hkl*). In contrast to regular von Laue reflections, the spots in the Fujiwara diffraction patterns are obtained in a divergent X-ray beam, have rather large dimensions, and represent the topograms of the crystal under study.

Clear and dark areas are clearly visible in the diffraction spots (topograms). One such diffraction spot is shown in Fig. 5. The photograph shows the boundaries of the blocks. An analysis of the geometry of these areas makes it possible to determine the size and shape of blocks, and the magnitude and sign of their misalignment within the sample.

By measuring the parameters of the shifts of the characteristic lines and the widths of the light and dark stripes at the boundaries of the blocks, and knowing the acquisition geometry, the magnitude and direction of misalignments of the blocks can be determined. The mechanism of the formation of such displacements can be understood from Fig. 6. In Fig. 6a, the reflected beams from the two blocks are separated and the block boundary is displayed as a light stripe in the topogram. In Fig. 6b, the orientation of the blocks is such that the beams are superimposed and the boundary is depicted by a dark stripe.

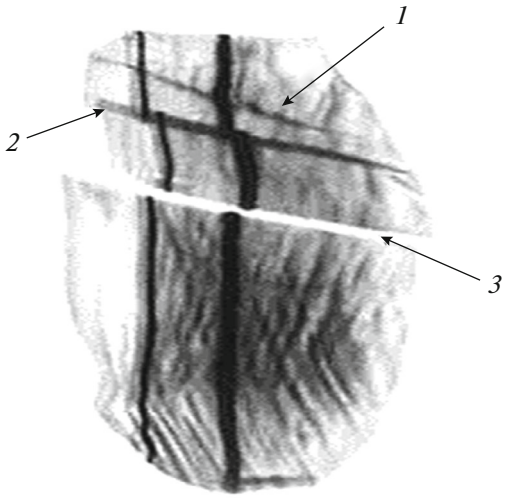

Fig. 5. One of the diffraction spots of the X-ray diffractogram obtained by Fujiwara's transmission method; this is the topogram of a sapphire single crystal, which is recorded under conditions when the distance from the X-ray source to the crystal is $A = 100$ mm and the distance from the crystal to the film is $B = 150$ mm; the vertical dark lines shifting at the boundaries of blocks are traces of the K_α and K_β characteristic diffraction lines; the light and dark bands (grain boundaries) marked by arrows *1*, *2*, and *3* and extending in the horizontal direction indicate that the crystal consists of at least three blocks misaligned with respect to each other [10].

BERG–BARRETT METHOD

A similar technique is used to analyze the topograms obtained from the Berg–Barrett geometry (Fig. 7). Monochromatic radiation in the form of an almost parallel beam incident on the crystal under a sliding angle to the surface is used in the Berg–Barrett scheme [7]. The recording photographic film is installed at the minimum possible distance from the sample and in the position parallel to the sample or perpendicular to the reflected beam. This method is usually used to study the surface of mono- or polycrystals and allows one to gain a general idea of the degree of crystal perfection. The size and shape of grains, and the misalignment angles can be determined from the recorded topogram, and preliminary information on the dislocation structure can be obtained.

The optical and X-ray topograms of a single crystal are shown in Fig. 8 [6]. The crystal for optical photography was specially etched in an acidic etching agent to form a relief associated with crystal defects. The small-angle interface and the pits of etching of dislocation points formed at the place of emergence of dislocations on the crystal surface are clearly visible in the optical topogram. The X-ray topogram (by the Berg–Barrett method) was recorded before treatment of the sample in acidic etching agent. It clearly shows elastic deformations near all defects.

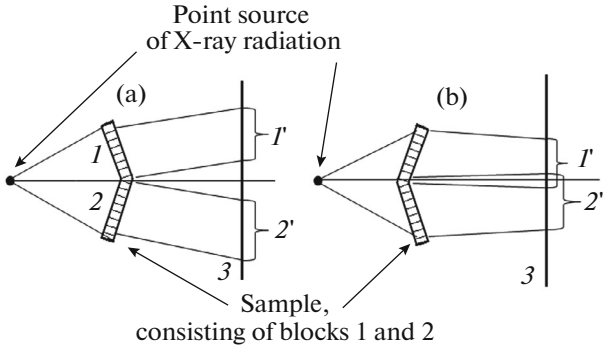

Fig. 6. Scheme illustrating the formation of light and dark boundary bands in topograms given in Fig. 5; the sample consists of two blocks 1 and 2 unfolded relative to each other by some angle; the grain boundary is the area of contact between the two blocks; projections *1'* and *2'* are produced by X-ray beams diffracted from blocks 1 and 2 on photographic film *3* recording the diffraction pattern; when the blocks are turned, the beams either (a) diverge forming a light stripe or (b) are superimposed forming a dark stripe.

SCHULZ METHOD

A point X-ray source is used in the Schulz scheme [8], and the X-ray image is obtained in white radiation (the polychromatic bremsstrahlung spectrum) (Fig. 9). The source–sample and the sample–film distances are usually 150 mm. This scheme is used to study block crystals. The rotations of blocks result in displacement of their images in the topogram, which makes it possible to calculate the rotation angles.

In the 1970s, the Schulz method used to analyze the degree of perfection of grown single crystals of refractory metals was improved, since long exposure times were required when shooting topograms because of the low intensity of the white spectrum. To increase the rapidity of the method, the use of an additional

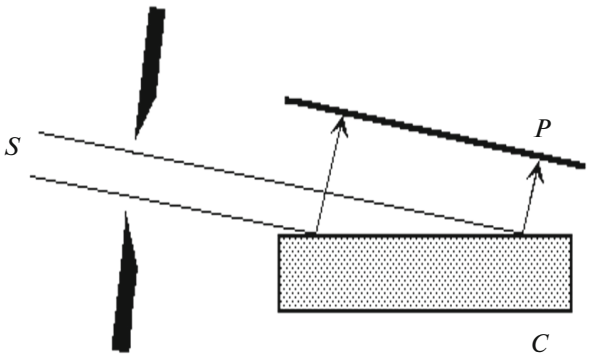

Fig. 7. Scheme of Berg–Barrett X-ray topography, where *S* is the X-ray source, *C* is the studied sample, and *P* is the photographic plate; a parallel X-ray beam is incident on the crystal at a grazing angle of 1°–5°, and the sample–film distance is usually 1–2 mm.

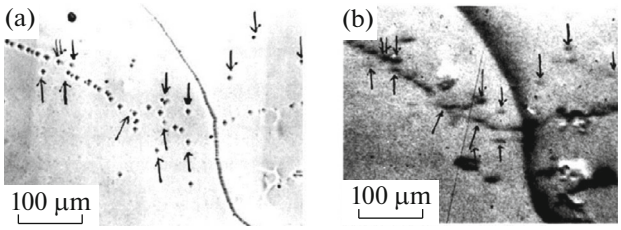

Fig. 8. (a) Optical and (b) X-ray topograms of a LiF crystal; etch pits are seen in the optical photograph at the points where the dislocations exit to the surface; local microstresses near the dislocations are clearly seen in the X-ray topogram taken by the Berg–Barrett method using CrK_α radiation and the (220) reflection [6].

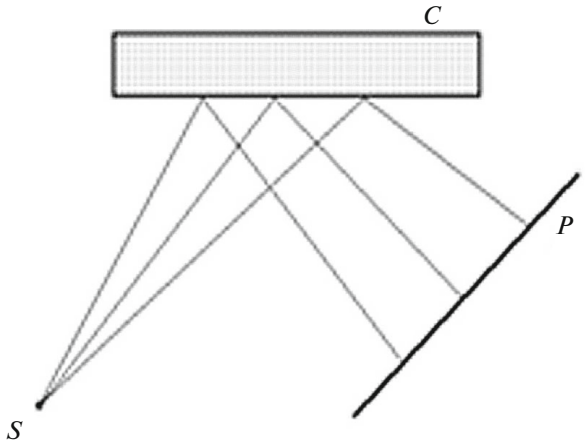

Fig. 9. Scheme of the Schulz geometry, where S is the point source of polychromatic X-ray radiation, C is the sample, and P is the photographic plate; the photographic film positioned approximately perpendicular to the reflected beams is at a distance of about 150 mm from the sample.

contribution of the characteristic spectrum when forming a topographic image by angular scanning of the sample and the film in a certain range of angles was suggested in [16]. The angular range of scanning was chosen in such a way that the characteristic part of the spectrum would be used in the formation of an image along with the white spectrum. As a result, the exposure time was significantly reduced.

The angular scanning scheme proposed in [16] is shown in Fig. 10. This method is called the topography of angular scanning. During exposure, the crystal rotates around the O_1 axis in the angular interval 2α at a speed of ω, and the film is involved in a complex motion that is made up of rotation around the O_1 axis at a speed of 2ω and around the O_2 axis at a speed of ω. As a result, the sample region ΔX_C is displayed in the topogram as ΔX_F. With this motion, the surface of the film remains parallel to the surface of the crystal, and the X-ray beam reflected at point O_1 is incident at the point O_2. With such scanning, the image of the crystal is composed of an image in polychromatic radiation (as in the Schulz method) and an image formed in the characteristic spectrum, which results in a shorter exposure time.

A number of studies on the structure of twin and interface boundaries in single crystals of KH_2PO_4, $LaGaO_3$, $YBa_2Cu_3O_{7-d}$, ZnS, $BaNiO_3$, etc. have been performed by the method of angular scanning [17–20].

The Berg–Barrett, Schulz, and Fujiwara methods are mainly used to observe large defects, such as grain boundaries. These schemes make it possible to determine the geometry, dimensions, and misalignment of the blocks, i.e., to study the substructure of crystals.

The considered methods imply that the radiation sources should be point-like. Otherwise, each point of the source will give its own image. Since all the beams are divergent, these pictures are superimposed and, as a result, the overall picture of the crystal image is blurred. The use of an extended X-ray source can significantly shorten the time for obtaining the topograms, but this is possible only if the X-ray source produces a parallel beam, i.e., almost a planar wave. In practice, this is implemented by using special monochromators or using the Borrmann effect.

BORRMANN METHOD

Let us review topographic techniques based on the Borrmann effect. This phenomenon was discovered experimentally by Borrmann in 1941 [14]. For some systems of planes, a noticeable decrease in absorption with a change in the thickness of the crystal is observed

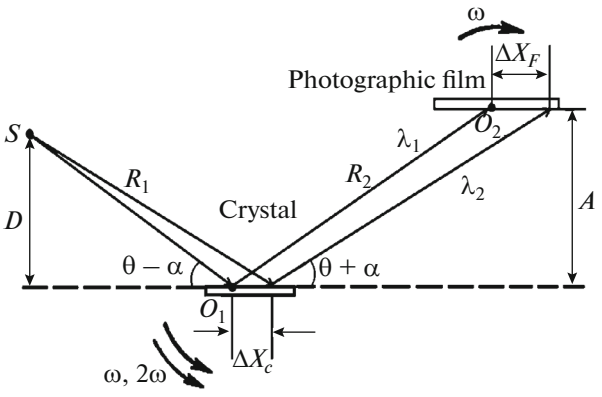

Fig. 10. Scheme of the angular scanning topography, where α is the angle of scanning, S is the source of polychromatic X-ray radiation, R_1 is the distance between the radiation source and point O_1 on the sample, R_2 is the distance between point O_1 on the sample and point O_2 on the film, D is the distance between the radiation source and the plane of the sample, and A is the distance between the plane of the sample and the plane of the film; an image of the ΔX_F crystal region recorded on the film; the image recorded on the film is formed by waves with lengths in the range between λ_1 and λ_2.

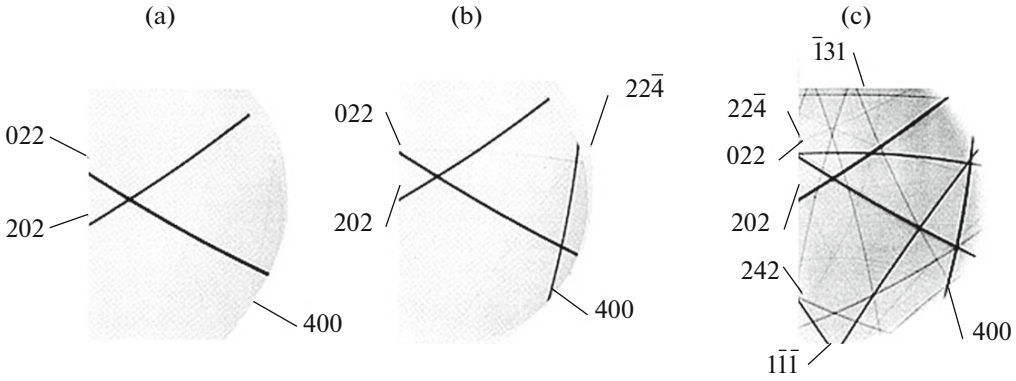

Fig. 11. Three topograms of a single Ge crystal, which are obtained using a point X-ray source in a divergent beam; the thickness of the crystal was reduced by mechanical and chemical polishing of the sample to the following values: (a) $t_1 = 1.2$ mm, (b) $t_2 = 0.5$ mm, and (c) $t_3 = 0.2$ mm [14]; the brightness of the lines of types (022) and (202) varies only slightly with a change in the thickness of the crystal.

in comparison with other reflecting planes when X-ray radiation passes through a crystal in the Bragg position. Three images of the same von Laue reflection obtained in a divergent X-ray beam from a point source of CuK_α radiation with a Ni filter that attenuates the β line is shown in Fig. 11 for a Ge single crystal. The thickness of the sample in the experiment was altered by mechanical and chemical polishing (1.2, 0.5, and 0.2 mm). Lines corresponding to the reflection of K_α radiation from different crystallographic planes (the plane indices are shown in Fig. 11) are observed in the diffraction spot. The experiment shows that the brightness of the lines of types (022) and (202) varies little with changing thickness of the crystal. The thickness, t, was 1.2, 0.5, and 0.2 mm, which corresponds to μt product values of 42, 17.5, and 8 (μ is the linear absorption coefficient). Furthermore, the brightness of other lines varies significantly, some lines simply disappear at a large crystal thickness. The observed lines of types (022) and (202) in this experiment are reflections from planes perpendicular to the crystal surface, i.e., this is the symmetric case of von Laue diffraction.

According to the dynamic theory of scattering, two coherent waves with close wave vectors propagate in the first approximation when diffraction occurs in the crystal lattice. They are called the "ordinary" and "anomalous" waves. The "ordinary" wave is absorbed fairly quickly, since it has an ordinary absorption coefficient. The "anomalous" wave has a significantly smaller absorption coefficient and passes through the crystal, being absorbed to a much lesser degree. Passing through the crystal, this wave gradually contracts into a thin ray inside the crystal. As a result, a parallel beam of rays is formed inside the crystal and on the way out of it, whereas a stripe from an extended radiation source is exposed on the crystal surface. Therefore, sufficiently clear X-ray topograms are obtained for thick crystals, even with an extended radiation source.

The above situation is illustrated in Fig. 12, in which computer simulation of the X-ray wave field inside the scattering triangle is shown. A triangle of scattering in diffraction physics is a triangle formed by direction of the wave vector, $\mathbf{K}_0$, of the incident wave, the direction of the wave vector, $\mathbf{K}_\mathbf{H}$, of the diffracted wave, and the diffraction vector, $\mathbf{H}_{hkl}$, perpendicular to the system of reflecting planes (hkl). Indenbom in his papers called this triangle the "Borrmann triangle" or the "Borrmann tent". The inset in Fig. 12 shows the wave field in the uppermost part of the scattering triangle, in which both waves propagate. They form a complex interference structure of the field. As the waves penetrate deep into the crystal, the ordinary wave is absorbed, and oscillations disappear. The remaining anomalous wave contracts to the center of the scattering triangle [21].

A topography scheme using the Borrmann effect is shown in Fig. 13. Obviously, each point of the focused X-ray source emits a spherical wave. However, the crystal chooses only that ray, for which the Wulff–Bragg condition is fulfilled, among all other rays. Next, not the entire base of the scattering triangle is exposed on the radiation-departure surface for a thick crystal, but only a narrow anomalous wave is formed at the center of the scattering triangle (the Borrmann effect). Therefore, almost parallel beams of diffracted and transmitted waves leave the crystal. These waves form a diffraction image of the defects that are present in the volume of the crystal and project it onto the radiation-departure surface. The diffracted and transmitted waves emerging from the crystal carry information about the images of these defects.

X-ray topography schemes based on the Borrmann effect make it possible to observe very fine details of the real structure of crystals in comparison with the Berg–Barrett, Schulz, and Fujiwara methods. First of

all, these are separate dislocations, clusters of point defects (clusters), twin boundaries, and electric and magnetic domains [22–34].

Two typical topograms taken using the Borrmann effect are shown in Fig. 14 [31]. The crystal has the shape of a rectangular prism. Two transmission topograms from two of its faces are obtained. The above images make it possible to obtain a three-dimensional reconstruction of the sample (tomography of the sample). Growth dislocations aligned approximately along the [111] growth axis and growth bands parallel to the (111) planes are clearly seen in Fig. 14b. Dislocation outcrops on the surface in the form of multipetal rosettes are seen in the upper topogram. There are two types of rosettes, namely, two-petal and multipetal rosettes, which indicates the presence of different dislocation types. Analysis shows that two-petal rosettes are images of screw dislocations, and multipetal ones are edge dislocations. Lines intersecting the crystal from top to bottom are observed in the lower topogram. These are dislocation lines, whose outcrops are visible in the upper topogram. It should be noted that the brightness of the lines is different (screw and edge dislocations). There are also bright horizontal bands—so-called "growth" bands, i.e., regions with variations in the density of impurity atoms—in the lower topogram. The crystal growth axis in this case is perpendicular to the growth bands.

METHODS FOR OBTAINING A QUASI-PLANAR WAVE

The use of asymmetric Bragg reflection from a perfect crystal is another method of obtaining a practically parallel beam [13, 35–37]. It is known from the kinematic theory of scattering that the divergence of a reflected wave in the Bragg geometry depends on the reflection asymmetry. The larger the angle between the surface of the crystal and the system of reflecting planes, the smaller the divergence of the reflected wave. This relationship is determined by the following expression:

$$\Delta\theta_{\mathbf{K}_1} = \frac{\sin(\theta - \alpha)}{\sin(\theta + \alpha)}\Delta\theta_{\mathbf{K}_0} = \gamma\Delta\theta_{\mathbf{K}_0}. \quad (3)$$

Here, α is the angle between the crystal surface and the system of reflecting planes; $\Delta\theta_{\mathbf{K}_0}$ and $\Delta\theta_{\mathbf{K}_1}$ are the divergences of the incident and diffracted waves, respectively; and γ is the asymmetry coefficient. Thus, the smaller the asymmetry coefficient, the smaller the divergence of the reflected beam. The parameters of the reflection geometry in the asymmetric case are schematically illustrated in Fig. 15.

Many different monochromator–collimator schemes are implemented with the use of this effect. One of these schemes is shown in Fig. 16. This is a single-crystal block, in which channels are cut for an X-ray beam and reflecting surfaces are polished. Collimated

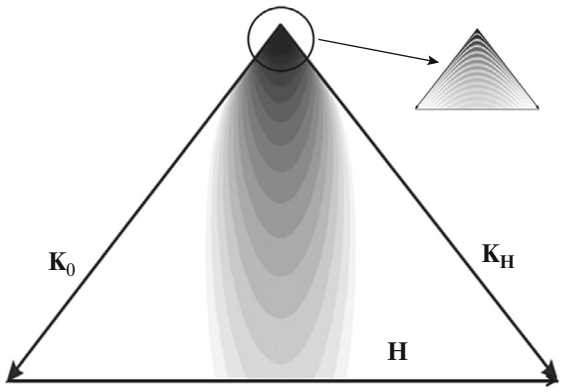

Fig. 12. Computer simulation of the wave field in the scattering triangle (numerical solution of the Takagi–Taupin equations) [21].

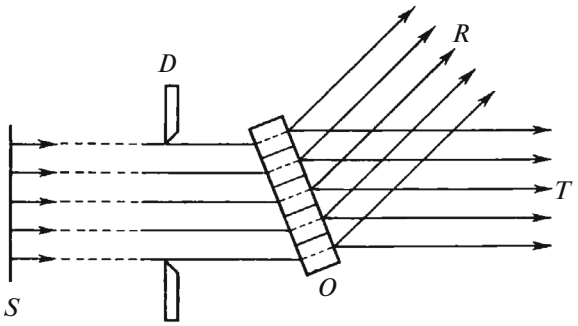

Fig. 13. Scheme illustrating the X-ray topography that uses the Borrmann effect, where *S* is an extended radiation source, *D* is the collimator gap, *O* is the sample (single-crystal plate), and *R* and *T* are diffracted and transmitted beams, respectively.

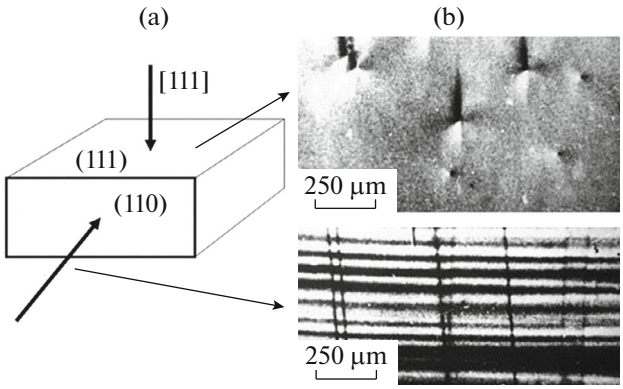

Fig. 14. (a) Silicon crystal in the form of a rectangular prism with a size of 10 × 5 × 3 mm; (b) the fragments of two topograms (stereo pair) obtained by reflection from planes (111) (the upper topogram) and (220) (the lower topogram) [31] by using CuK_α radiation; the crystal growth axis coincides with the [111] direction.

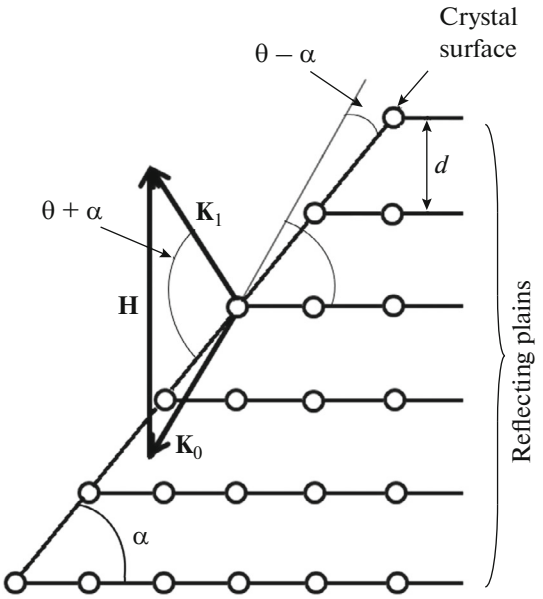

Fig. 15. Scheme explaining the asymmetric Bragg reflection, where $\mathbf{K}_0$ and $\mathbf{K}_1$ are, respectively, the wave vectors of the incident and reflected waves, θ is the diffraction angle, *d* is the interplanar distance, and α is the asymmetry angle.

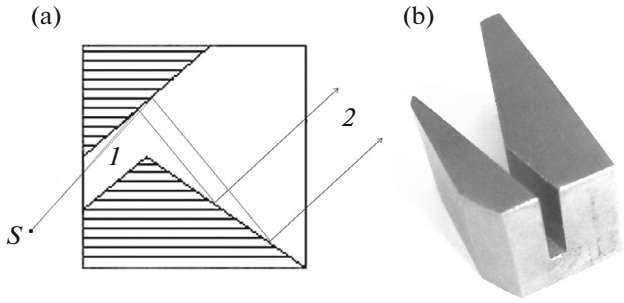

Fig. 16. (a) Scheme of a monochromator creating a quasi-planar wave considered in [13, 35], where the horizontal lines in the crystalline blocks are reflecting planes, *1* is the spherical (divergent) wave from source *S*, and *2* is the quasi-planar wave after the second asymmetric reflection; (b) a photograph (exterior view) of one of the crystal monochromators.

divergent beam *1* from a point source is transformed into quasi-planar wave *2* with a divergence of tenths of an angular second as a result of double asymmetric reflection.

LANG METHOD

In 1959, Lang proposed a fundamentally new scheme for obtaining X-ray topograms (scanning, limited, and sectional topograms) [15]. It was this method that initiated the study of the physics of the diffraction imaging of crystal-lattice defects. The Lang scheme for obtaining topograms is shown in Fig. 17. In the Lang method, a thin collimated X-ray beam from point source *S* is incident onto single-crystal sample *C* through collimator K_1. The crystal is placed in the reflection position for the selected system of reflecting planes (*hkl*) in such a way that $K_{\alpha 1}$ radiation is reflected. Then, a diffracted or transmitted beam is selected using slit K_2 and detected by detector *D*. The crystal and the detector are mounted on a special device that can move the sample and the detector back-and-forth under the X-ray beam without violating the Bragg condition. In this case, the detector will detect the diffraction image of a necessary part of the crystal within the range of scanning.

One of the first X-ray topograms of a silicon single crystal, which is obtained by the method under consideration and published by Lang in [36], is shown in Fig. 18. The topogram shows many images of various defects, such as: thin black lines, including a spiral in the lower part of the topogram (the Frank–Read source), which is arisen from single growth dislocations, and wide dark areas arisen from dislocation clusters; parallel bands along the edges of the crystal—these are extinction contours known in optics as bands of equal thickness. The mechanism of the formation of such bands in X-ray topography differs from the mechanism of the formation of similar bands in optics.

The Lang method is widely used in studying the real structure of single-crystal silicon plates used in the electronics industry for the production of semiconductor chips. Defects in semiconductor crystals strongly affect the characteristics of electronic devices, so it is important to know what defects are present in the used samples, and what are their concentration and spatial location. All this information for large plates (up to 10 cm^2) can be obtained by the Lang method.

In the case of dislocations, it is known that they create local highly anisotropic distortions of the crystal lattice. The largest distortions are usually concentrated in the direction of the Burgers vector. Therefore, the maximum contrast on diffraction topograms is observed when reflected from the most distorted planes (distortions perpendicular to the reflecting planes), i.e., when the Burgers vector is perpendicular to the reflecting plane, and the condition that the scalar product of the Burgers vector and the diffraction vector is equal to unity, i.e., $(\mathbf{Hb}) = 1$, is satisfied. The contrast is minimal when reflection occurs from the planes, in which the Burgers vector lies, i.e., $(\mathbf{Hb}) = 0$. Here, **H** is the diffraction vector, and **b** is the Burgers vector of the dislocation. This is the main rule and an extremely simple one that makes it possible to determine the type of distortion from the extinction (disappearance) of the contrast of defects in some reflections [1–3]. The rule is general in nature and is applicable to almost all topographic methods. The mechanism, by which this rule operates, is illustrated in Fig. 19.

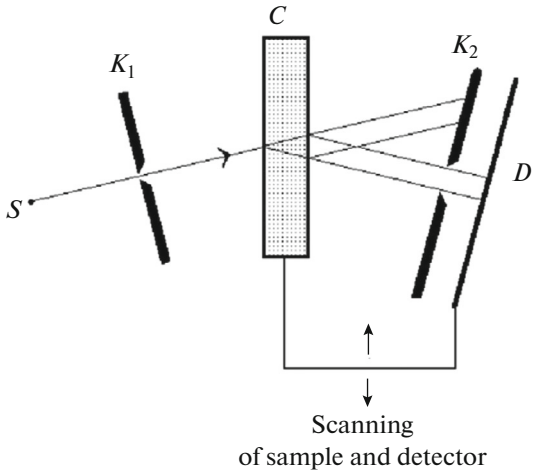

Fig. 17. X-ray scheme of the Lang method, where S is the point source of X-ray radiation, C is the sample (single crystal), D is the detector (photographic plate) recording the obtained X-ray topogram, and K_1 and K_2 are collimators; simultaneous movement (scanning) of the sample and detector allows one to record large areas of the crystal under study.

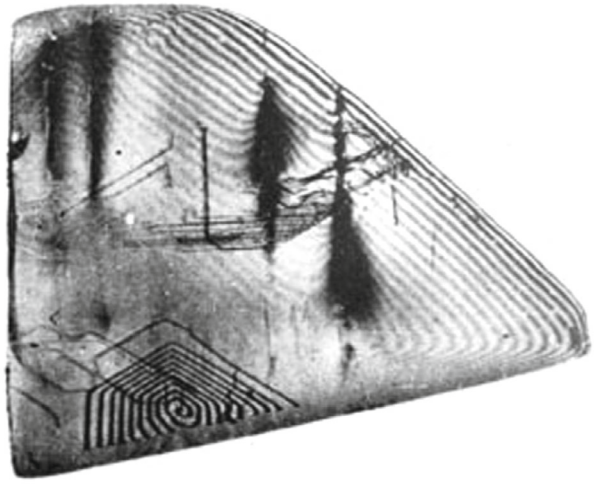

Fig. 18. X-ray topogram of a single Si crystal obtained by the Lang method [36], where the thin black lines, including the spiral line, are single dislocations, the wide dark areas are dislocation clusters, and the parallel stripes along the edges of the crystal are extinction contours or X-ray bands of equal thickness.

Four typical topograms obtained by the Lang method on four different samples are shown in Fig. 20. The projection topogram of a silicon single crystal with growth dislocations is shown in Fig. 20a [37]. The conditions are as follows: the (111) crystal surface; the (220) reflection; MoK_α radiation; and the crystal thickness is 800 μm ($\mu t \approx 1.1$). The topogram of a silicon single crystal with dislocation loops emerging from a stress concentrator on the sample surface (scratch) during deformation of the sample at a temperature of 600°C is shown in Fig. 20b [38]. The conditions are as follows: the thickness of the crystal is 300 μm; the (111) surface; MoK_α radiation; and the long edge of the loop is oriented along the [110] direction. The topogram of a silicon single crystal after lithography is shown in Fig. 20c [39]. The fragments of four microcircuits, one of which is marked with a white circle, and also the inclined comet-like lines of growth dislocations are clearly visible in the topogram. Finally, the topogram of a single crystal of iron–yttrium garnet with the image of 180° magnetic domains is shown in Fig. 20d. The conditions are as follows: AgK_α radiation; the (800) reflection; and the crystal thickness is 180 μm [40].

SECTIONAL TOPOGRAPHY

If scanning in the Lang scheme is stopped, then the recorded still-frame is called the sectional topogram. Topograms obtained with scanning are called projection topograms. Sectional topograms are widely used to obtain numerous quantitative characteristics of defects, such as the type of defects, the depth of their occurrence below the surface of the sample, the intensity of local elastic lattice distortions associated with defects, etc. The analysis of sectional topograms makes it possible to find out how the diffraction image of a defect is formed and what quantitative information can be extracted from the structure of the diffraction image [41–45]. A typical example of the sectional topogram depicting a dislocation inclined to the sample surface is shown in Fig. 21.

The bands observed at the edges of the sectional topogram are formed as a result of the interference of ordinary and anomalous waves propagating inside the scattering triangle. In order to observe interference fringes in sectional topograms, it is required that the width of the front of the X-ray beam incident on the

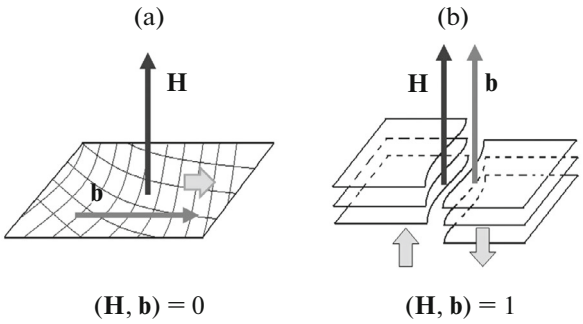

Fig. 19. Rule for determining the direction of the Burgers vector of dislocations is illustrated schematically for the cases (a) when the distortions are concentrated in the reflecting plane and the image of the defect should be absent at **(Hb)** = 0, and (b) when the distortions are located perpendicular to the reflecting plane and the image of the defect should have the maximum brightness at **(Hb)** = 1.

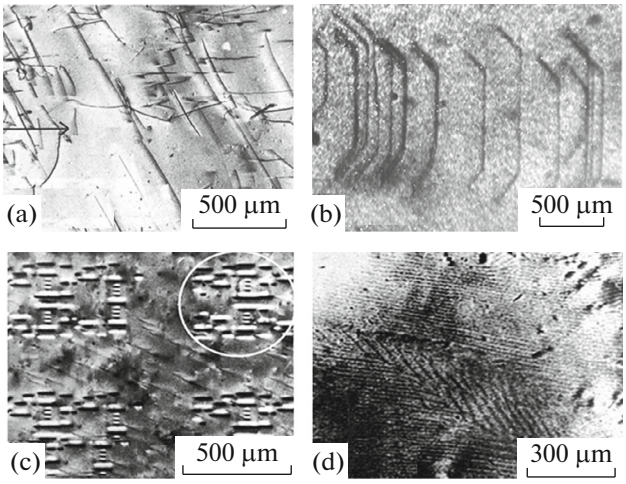

Fig. 20. Projection X-ray topographs obtained by the Lang method for (a) growth dislocations in a silicon single crystal [37], (b) dislocation half-loops introduced into a silicon single crystal under plastic bending [38], (c) a fragment of the X-ray topogram with lithography of four prospect microcircuits [39], and (d) a fragment of the X-ray topogram of a single crystal of iron–yttrium garnet with the image of magnetic 180° domains [40].

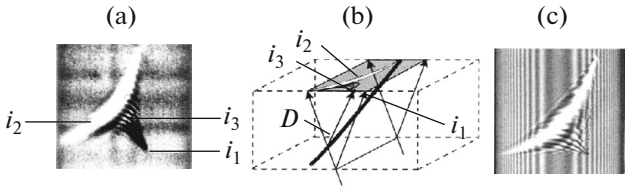

Fig. 21. (a) Experimental sectional image of a dislocation positioned obliquely in a silicon sample having the shape of a parallelepiped; the image is obtained using a Mo$K_{\alpha 1}$ radiation source, a crystal thickness of 0.8 mm, $\mu t = 1.12$, and the (220) reflection; (b) a schematic representation of a crystal with a defect, where i_1 is the direct image, i_2 is the dynamic image, and i_3 is the intermediate image; (c) numerical simulation of the sectional X-ray topogram corresponding to the above images [43].

crystal ensure scattering inside the scattering triangle, on the one hand, and be smaller than the width of the interference fringes observed at crystal exit, on the other hand. Usually, the width of this front is 5–10 μm. Methods for the quantitative analysis of local elastic deformations of the crystal lattice by using sectional topograms were suggested in the works of Kato, Otier, and Indenbom, which were used to study defects in silicon single crystals [21, 37, 46–50]. These methods are based on the shift of interference fringes in the local elastic field of the defect. In turn, the bending is determined from the magnitude and shape of the elastic deformation field associated with the field of the defect.

A sectional X-ray topogram obtained on a silicon crystal with an oxide film is shown in Fig. 22. The X-ray beam falls on the edge of the oxide film. The elastic field arising from the interaction of the film edge with a single crystal is manifested in the sectional topogram in the form of a shift in the interference fringes formed in the scattering triangle. The shape and magnitude of the band displacements can be used to determine the numerical values of the elastic-field parameters.

Sectional X-ray topograms of silicon single crystals are shown in Fig. 23. A sectional topogram with a single screw dislocation intersecting the scattering triangle along the diffraction vector is shown in Fig. 23a; the scheme for obtaining a sectional topogram is shown in Fig. 23b; and a topogram with the image of a weak defect (as a rule, these are macrodefects with dimensions up to 1 cm, the elastic field of which does not form a direct image of the defect, but only displaces the interference fringes near the defect) is shown in Fig. 23c.

RESOLUTION OF X-RAY TOPOGRAPHY METHODS

The linear resolution in X-ray topography methods is usually low, namely, around a few micrometers, and is mainly determined by the following three factors: the divergence of the incident beam, the spectral width of the used radiation line, and diffraction broadening of the image [2, 3, 43].

The plane, in which the incident and diffracted beams lie, is called the plane of scattering. In accordance with the Bragg formula, the divergence of a beam with a width of $\delta\lambda_d$ is determined by the relation, $\delta\theta_d > \tan\theta \times \frac{\delta\lambda_d}{\lambda_d}$. In the case when the divergence of the beam incident on the crystal is large, i.e., $\delta\theta_i > \tan\theta \times \delta\lambda_i/\lambda$ (here, $\delta\lambda_i$ is the spectral width of the beam incident on the crystal), the divergence, $\delta\theta_d$, of the diffracted beam is limited, in accordance with the Bragg relation, by the spectral width of the radiation beam incident on the crystal. This case is usually implemented when recording in monochromatic radiation, for example, in characteristic K_α radiation.

The divergence of the incident wave is determined by the geometry of the experiment and can be written in the form, $\delta\theta_i = \delta x/L$, where δx is the source size in the scattering plane and L is the distance from the source to the crystal. For example, when topograms are recorded in "white" radiation and using a microfocus source, the opposite relation is often satisfied, that is, $\delta\theta_i < \tan\theta \times \delta\lambda_i/\lambda$. In this case, the divergence, $\delta\theta_d$, of the diffracted beam is equal to the divergence, $\delta\theta_i$, of the incident wave, and its spectral width, $\delta\lambda_d$, is given by the Bragg relation. The spatial resolution in the scattering plane is determined in the topogram by the simultaneous action of the following two factors: geometric and diffraction broadenings. The geometric

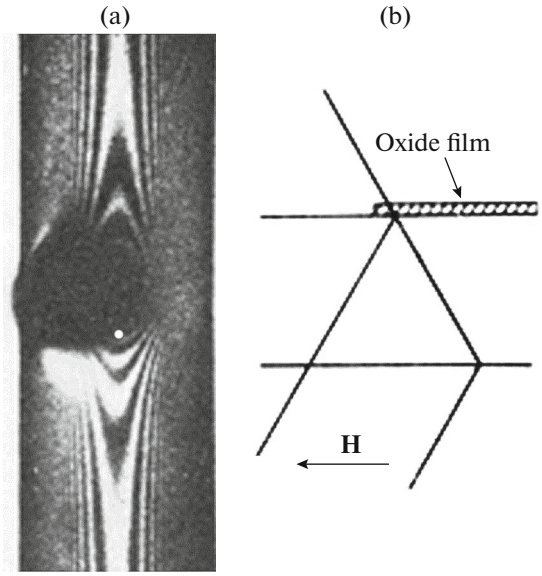

Fig. 22. Sectional X-ray topogram obtained at the edge of an oxide film formed on the surface of a silicon single crystal; (a) the interference fringes are curved near the edge of the oxide film, since the film deforms the single crystal underneath it; (b) scheme of the experiment [47].

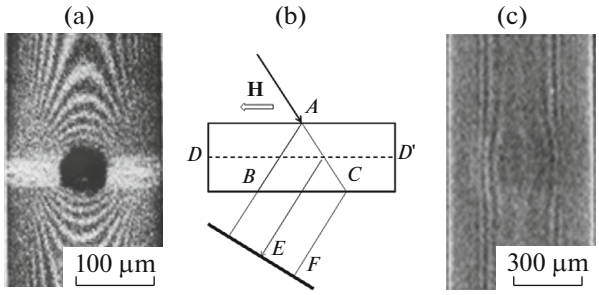

Fig. 23. (a) Sectional X-ray topogram of a silicon single crystal with the *DD*' rectilinear helical dislocation, which crosses the entire crystal and the *ABC* scattering triangle; (b) scheme of the experiment [48]; (c) sectional X-ray topogram of a silicon single crystal with a defect, the elastic-field strength of which is not sufficient to form a direct image of the defect [49–51].

broadening is equal to $\delta x = \delta\theta_d \times l$, where l is the distance from the crystal to the photographic plate, and the $\delta\theta_d$ value is determined either by the monochromaticity or the divergence of the incident beam.

The diffraction broadening is described by the dynamic theory of X-ray scattering and can be estimated as $\Lambda \times \cot\theta$, where $\Lambda = \dfrac{\lambda\cos\theta}{C\chi_{hkl}}$ is the extinction length, χ_{hkl} is the Fourier component of the crystal polarizability corresponding to atomic planes with Miller indices (hkl), and the C coefficient equals $\cos 2\theta$ for polarization in the scattering plane (π-polarization) and 1 for polarization in the plane perpendicular to it (σ-polarization). The resolution in the direction perpendicular to the scattering plane is determined by geometric broadening, as follows: $y_g = \delta y \times l/L$. There is another factor that greatly affects the resolution of X-ray topography methods—this is the resolving power of the recording X-ray detectors. The resolution is limited by the resolving power of the detector, which usually does not exceed 250–500 line/mm for the case of photographic plates. When high-resolution photoemulsions are used, the combined effect of all factors makes it possible to obtain images with a resolution of about 2.0–5.0 μm.

METHODS FOR INCREASING THE BRIGHTNESS OF X-RAY SOURCES: SYNCHROTRON RADIATION

The main drawback of X-ray topography techniques, in particular the Lang method, is the long duration of exposure, which can range from several hours for topograms with scans up to tens and even hundreds of hours for high-resolution sectional topography images. The exposure time depends on the area of scanning, the X-ray radiation source power, and the detector type. The fact is that the energy efficiency ratio of traditional X-ray sources (X-ray tubes) is tenths of a percent. Thus, the efficiency coefficient of an X-ray tube with a copper anode at an applied voltage of 30 kV and a current of 10 mA (the ratio of the expended energy to the energy of the X-ray beam) is only about 0.2%. The problem of increasing the brightness of X-ray sources in different years was solved in different ways. In the 1960s, sources with rotating anodes have been developed to increase the current of the X-ray tube. This made it possible to substantially increase the dissipated power at the anode and, as a result, the tube current. Japanese firm Rigaku has released a whole line of RU-200, RU-500, and RU-1000 units (the tube currents are 200, 500, and 1000 mA respectively). At that time, the ARTVA-2 and ARTVA-5 devices with tube currents of 80 and 200 mA, respectively, were developed in the former Soviet Union by SKB RA enterprise (Special Design Bureau for the development of X-ray equipment) in union with the Burevestnik factory (St. Petersburg). However, these X-ray sources were not commercialized due to the complexity of operation and high cost.

Another area is associated with the creation of specialized electron accelerators/synchrotrons, in which the brightness of the X-ray beam can be increased by 10 or more orders of magnitude [52–57]. It is shown in Fig. 24, how the brightness of X-ray sources has changed over the past 100 years. The physics of synchrotron radiation is based on the known corollary of Maxwell theory that any charged particle moving with acceleration emits electromagnetic waves (Larmor radiation). If a charged particle (electron) moving in a closed orbit in an accelerator is deflected back and forth from the stationary orbit, for example, following

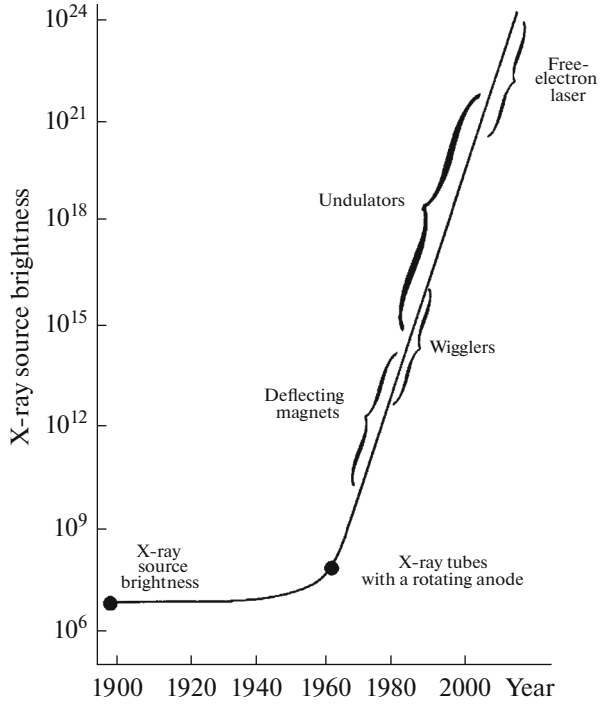

Fig. 24. Changes in the brightness of X-ray radiation sources during the period from 1900 to 2000 [53].

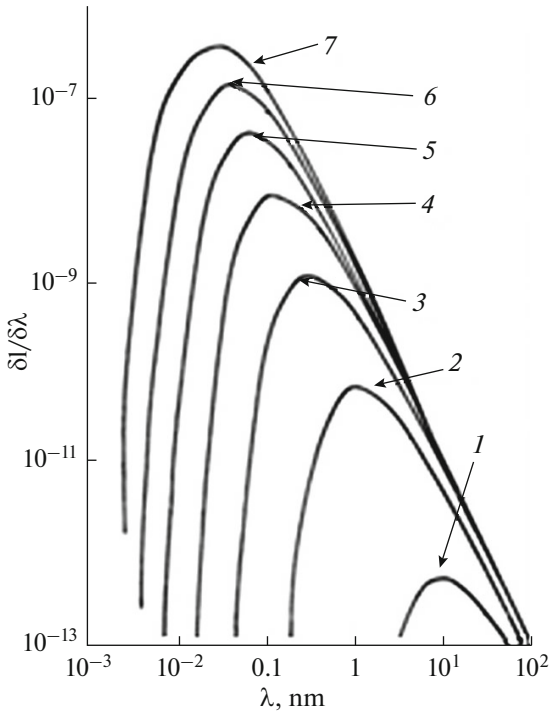

Fig. 25. X-ray radiation spectrum of the DESY synchrotron in Hamburg for different electron energies equal to 1.1 (*1*), 2.0 (*2*), 3.0 (*3*), 4.0 (*4*), 5.0 (*5*), 5.9 (*6*), and 7.2 (*7*) GeV in the accelerator ring [54]; the ordinate shows the spectral brightness of the X-ray radiation.

a sinusoidal law, this should lead to the emergence of normal acceleration of the alternating sign, which is accompanied by the additional emission of electromagnetic waves. To increase the brightness of X-ray radiation in synchrotrons, magnets deflecting the electron beam were first used; then special devices, namely, wigglers and undulators were developed, which made it possible to sharply increase the brightness of X-ray radiation sources by 10 or more orders of magnitude. At present, even more powerful X-ray sources, namely, free-electron lasers have been developed and are being constructed [56].

At present, there are several synchrotron research centers in the world. As a rule, these are centers of broad scientific specialization (X-ray optics, materials science, biology, medicine, chemistry, etc.). The largest and most renowned centers in Europe are ESRF in Grenoble (France), DESY near Hamburg (Germany), and the Kurchatov Source of Synchrotron Radiation at the Research Center Kurchatov Institute in Moscow (Russia) [53, 55, 56].

The X-ray spectrum in synchrotrons is continuous. The typical spectrum of a synchrotron source is shown in Fig. 25. The wavelength at the distribution maximum can be estimated from the following relation:

$$\lambda_{\max} \approx \frac{4\pi m_e c}{eH}\left(\frac{m_e c^2}{E_e}\right)^2. \quad (4)$$

Here m_e is the electron mass, c is the speed of light, e is the elementary charge, H is the magnetic-field strength, and E_e is the energy of electrons in the accelerator ring. With an increase in the energy of electrons, the distribution maximum shifts into the region of shorter wavelengths.

The use of powerful radiation sources opens up new horizons in X-ray topography. Firstly, the exposure time of topograms is reduced (to a dozen seconds). It becomes possible to use double- and triple-crystal topography, which greatly increases the sensitivity of the technique to local crystal-lattice distortions. One more very important feature is added, namely: it becomes possible to investigate the processes occurring in the studied samples in real time. Synchrotron radiation has several advantages over conventional laboratory sources, the most important of which are the total polarization of radiation in the electron-orbit plane and a very small divergence of the X-ray beam (from fractions of an angular second to several seconds, depending on the accelerator parameters). The continuity of the spectrum, a large cross section of the X-ray beam, and the small divergence make it possible to perform unique synchrotron studies of the structural perfection of crystals, in particular, to obtain original Fujiwara diffraction patterns, each spot of which is a topogram of the crystal [57].

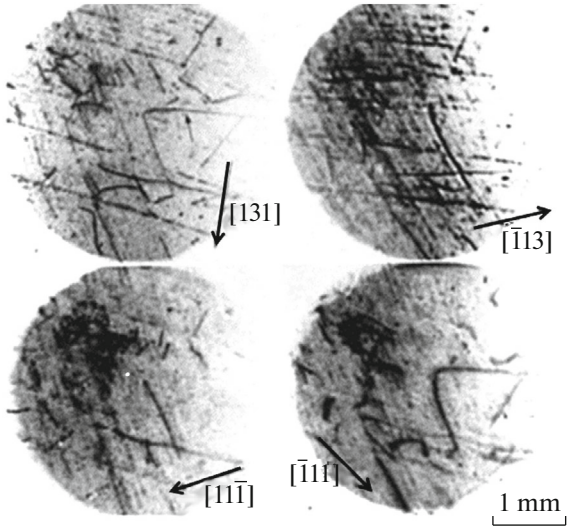

Fig. 26. Fragments of synchrotopograms of a silicon single crystal; the thickness of the single crystal is 3.5 mm, the energy of electrons in the ring is 7.2 GeV, the current in the ring is 7 mA, and the exposure time is 40 s; the arrows show the normals to the reflecting planes [57].

Thus, a whole set of topograms corresponding to reflections from planes with different indices (*hkl*) can be obtained simultaneously.

Four such topograms are shown in Fig. 26, in which growth dislocations are clearly visible [57]. As is seen, the images of some dislocations fade away in certain reflections. Comparison of such reflections allows one to determine the type of these dislocations and the orientation of the Burgers vector from the extinction of contrast. More than 15 strong reflections can be observed simultaneously. The exposure time for obtaining all the topograms is 40 s, while it takes about 10–30 h to obtain one such topogram in a laboratory X-ray machine (40 kV, 15 mA). Analysis of the topograms obtained with a synchrotron allows us to almost fully describe the real crystal structure.

DOUBLE-CRYSTAL TOPOGRAPHY

In the 90s of the last century, double- and triple-crystal schemes of X-ray topography were widely used. This became possible mainly due to the use of powerful synchrotron radiation. Among the range of multicrystal techniques, the pseudoplanar-wave topography method is of special importance [58–60]. This is one of the most sensitive methods for studying local microstresses in crystals. It is these methods that made it possible not only to see, but also to quantitatively study the structure of complex defects in single crystals. The point is that it is rather difficult to analyze the diffraction image in single-crystal X-ray topography (diffractometry) because of the imposition of a number of factors, such as the width of the used spectrum,

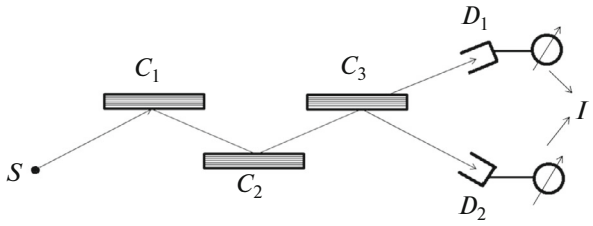

Fig. 27. Scheme of a triple-crystal X-ray spectrometer, where S is the X-ray radiation source, C_1 is the crystal monochromator, C_2 is the studied crystal, C_3 is the crystal analyzer; the C_3 crystal is absent in a two-crystal scheme, and the intensity of the diffracted beams is detected by detector D_1; D_2 is the detector of the triple-crystal scheme, and I is the intensity of the diffracted beam.

the size of the X-ray source, and the geometry used for obtaining the X-ray topogram. If the direct problem of obtaining a diffraction image of a defect by numerical simulation (solving the Takagi–Taupin equations) is solved quite easily for a known field of combined distortion, then the inverse problem of determining the field of combined distortion of the lattice associated with the defect seems to be quite complex and, therefore, it is difficult to decipher the diffraction image object [59]. The use of double-crystal and, especially, triple-crystal topography in a number of cases makes it possible to avoid these problems. The operating scheme of such a device is given in Fig. 27.

Crystal monochromators makes it possible to reduce the divergence of the incident beam in some geometry to an almost planar wave with a divergence in fractions of an angular second and improve the angular resolution. On the other hand, crystal monochromators significantly reduce the width of the spectrum of the created image [59]. The use of a crystal analyzer makes it possible to investigate the angular spectrum of rays diffracted at the sample. As a whole, all of this makes it possible to obtain images of defects without the distortion associated with X-ray beam divergence, the dimensions of the focal spot, and the spectral interval of the wavelengths involved in the formation of the image. In turn, this makes it possible to analyze the experimental and calculated images and, consequently, to determine the local deformation fields of crystal-lattice defects more reliably.

Transmission double-crystal synchrotron topograms of a germanium crystal are shown in Fig. 28, which are obtained for the reflection (111) at $\lambda \approx 0.35$ Å with a silicon (111) crystal monochromator. Growth dislocations, scratches, and discharges are visible. Two topograms shown in Fig. 28 were obtained for the following two crystal positions in the region of the Bragg reflection: the topogram given in Fig. 28a corresponds to the position of the crystal at the maximum intensity in the reflection curve; the topogram given in Fig. 28b corresponds to the position of the crystal deviated

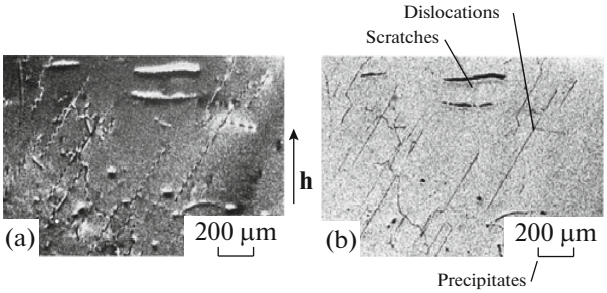

Fig. 28. Double-crystal X-ray topograms of a single germanium crystal obtained with synchrotron radiation [43, 60], as follows: (a) the X-ray topogram of the crystal at the operating point set at the top of the swing curve; dynamic and intermediate images of defects are observed; (b) the X-ray topogram of the same crystal section set in the middle of the swing curve slope; images of dislocations are narrowed and direct images predominate; the arrow between the photographs shows the direction of the diffraction vector.

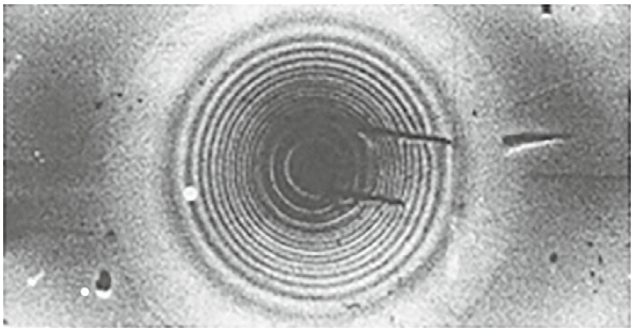

Fig. 29. Stroboscopic X-ray topography in synchrotron radiation; a quartz resonator is attached at the center of the crystal [43, 61].

from the exact Bragg position by a distance equal to half the width of the reflection curve. Analysis of the topograms makes it possible to understand how the dislocations are positioned in the volume of the crystal. For example, oscillations at dislocation lines give information on the tilt of these lines to the surface of the crystal. Measurements of the oscillation periods make it possible to determine the value of the inclination angle of the dislocation lines to the surface of the crystal. But most importantly, multicrystal topography makes it possible to investigate the angular structure of an X-ray beam diffracted at the studied sample on account of rotations of the crystal analyzer and the sample under study in a certain range of angles. This makes it possible to investigate in detail the structure of local deformations associated with defects in the crystal lattice. However, it should be emphasized that the use of multicrystal topography is possible predominantly with powerful X-ray sources because of a significant increase in the exposure time.

Reducing the time of the experiment when working on a synchrotron opens up another possibility, namely, real-time experiments. A stroboscopic topogram depicting a surface ultrasonic wave excited by a quartz resonator attached at the center of the crystal is shown in Fig. 29 [43, 61]. Contours of equal deformations of ultrasonic oscillations on the crystal surface are seen in the topogram.

EQUIPMENT USED IN X-RAY TOPOGRAPHY

In the early stages of the development of X-ray topography, various goniometers and geodetic theodolites were used to produce topograms. In the 1970s, the Japanese company Rigaku developed, for the first time, a special device on the basis of a D4-C microfocus X-ray source (the focus size is 20×30 μm^2, the tube current is 1 mA, and the voltage is 50 kV) with an A-3 special single-crystal spectrometer designed to produce X-ray topograms [39]. It was quite a versatile device that allowed the solution of many problems of X-ray topography. In the 1980s, several companies began to produce specialized instruments for X-ray topography. In the former Soviet Union, the Special Design Bureau of the Institute of Crystallography, Academy of Sciences of the USSR, prepared an experimental batch of DTS-1 and DTS-2 devices (double-crystal topographic spectrometers), TRS-1 and TRS-2 (triple-crystal X-ray spectrometers), later produced in St. Petersburg by the Burevestnik factory [62].

In recent years, many companies have produced universal X-ray diffractometers, which are easily rearranged for a variety of radiography tasks. The most interesting modern instruments for X-ray topography are described below.

The D8 Discover diffractometer (Bruker) has a modular architecture and can easily be rearranged into a wide range of different configurations, which makes it a very versatile tool for physical materials science.

The XRT-100 X-ray unit for X-ray topographic studies (RIGAKU/Fuji-Film) is a universal X-ray measuring system, which enables the experiment geometry to be changed and is equipped with a set of monochromators, collimators, and detectors. The goniometer allows one to use the single-, double-, and triple-crystal geometry of the experiment.

The CAD-4 X-ray diffractometer (Enraf-Nonius) is designed to solve a wide range of X-ray diffractometry problems when studying single crystals of large dimensions.

The DRON-7.0 X-ray diffractometer (Burevestnik) allows one to solve the problems of studying the real structure of single crystals.

In recent years, developments that allow one to avoid the mechanical control of X-ray goniometers have appeared. X-ray optical schemes and components of X-ray acoustooptics are being developed, which enable the main X-ray beam parameters in the experiment, such as the direction of propagation and

the wavelength, to be controlled. Ultrasound control makes it possible to rearrange the X-ray optical scheme with a high accuracy and a speed exceeding that of mechanical systems by several orders of magnitude. Laboratory samples of an X-ray diffractometer based on X-ray acoustooptics are described [63, 64], which enable rapid rearrangement of the X-ray optical scheme and measurement of the time-resolved diffraction reflection curve.

METHODS OF RECORDING AND ANALYSIS OF TOPOGRAMS

Traditionally, X-ray sensitive photographic materials have been mainly used to record X-ray images since the discovery of X-rays up the present day. The main drawback of photographic methods for recording X-ray images, on the one hand, is the long duration of the experiment (accumulation of exposure) and, on the other hand, a complex and prolonged photochemical process (it takes dozens of hours for thick-layer emulsions). The main advantage of photographic methods is a high linear resolution (around 2–5 μm), which is not currently achievable for other recording methods, and a relatively low cost. However, the situation has changed in recent years.

All currently used methods for recording and storing X-ray images can be divided into the following two groups: analog methods and digital methods. Detectors of the analog type are as follows: X-ray sensitive photographic films and photographic plates; specialized X-ray sensitive Vidicons (television systems); equipment using electron-optical image intensifiers (EOPs) [65–68]; and recording systems based on memory displays (plates with optical memory, Imag Plate) widely used in medicine [69, 70]. This technique allows one to reach a resolution of around 20–50 μm.

Another group includes digital detectors based on CCD (charge-coupled device) matrices. The CCD detector is a complex device on the basis of an integrated microcircuit consisting of a matrix of photosensitive or X-ray sensitive photodiodes [70, 71]. The method of the formation of an X-ray image distinguishes detectors of the direct and indirect conversion of X-rays into an electrical signal. In indirect-conversion detectors, X-ray radiation first enters a cesium iodide (CsI) or gadolinium oxysulfate (Gd_2O_2S) scintillator layer, in which it is converted into light quanta. Either a fiber optic block (an assembly comprised of millions of parallel glass fibers) or a microchannel plate (MCP), which transmits a pattern of light quanta to an integrated photodiode matrix converting light quanta into electrical signals, is usually located behind the scintillator layer. Fiber optics and MCP allow one to increase the resolution and to increase the brightness of the image. Microchannel plates are assembled from a large number (several million) of glass tubes with a diameter of 10–15 μm. The inner surface of these capillaries forms a microscopic electron multiplier due to special coatings, and the entire MCP becomes an image brightness intensifier.

Electron–hole pairs are directly generated in direct conversion detectors in the depth of a semiconductor matrix when X-ray quanta are applied. However, the linear resolution of all these systems so far is 10–15 μm at best. This resolution is sufficient in a number of cases, for example, when recording von Laue X-ray diffraction patterns or when obtaining survey images of crystal structure defects. However, one diffraction spot (with subsequent optical magnification) is required to be recorded in X-ray topography, and this resolution is not sufficient when studying the fine details of the diffraction image of defects. Among the numerous kinds of CCD detectors currently being produced by different companies, the following detectors used in X-ray topography should be mentioned:

(i) the high-resolution X-ray CCD camera (Very High Resolution X-Ray CCD-Camera Arrays, Photonic Science, France). This detector has an input window with a size of 124 × 83 mm^2 (a matrix of 4008 × 2672 pixels with a pixel size of about 31 μm);

(ii) high-sensitivity X-ray video detector (High-Sensitivity X-Ray Imaging System, Rigaku, Japan). The detector has an input window with a size of 14.75 × 9.42 mm^2 (a matrix of 1280 × 1024 pixels with a pixel size of about 15 μm).

The main problem of such systems is a high market price.

In X-ray topography, when it is required to investigate the details of the structure of a diffraction image and to compare them with images of numerical simulation, we still have to use the photographic method. As a rule, X-ray topography methods do not allow one to obtain an enlarged image of objects directly in the process of X-ray photography (the refractive index of X-ray radiation in any substance differs from unity in the sixth decimal place), so a recorded topogram containing images of microdefects with a size of about 1 μm (for example, dislocations and clusters) should be magnified by optical methods. Therefore, it is necessary to use techniques with sufficient resolution for recording X-ray topograms.

When the photographic recording of X-ray radiation is used, several mutually exclusive problems arise. To obtain reasonable exposure times, it is necessary to increase, on the one hand, the thickness of the emulsion layer and, on the other hand, the number and dimensions of X-ray sensitive grains, since X-rays have a relatively small absorption coefficient, i.e., weakly interact with the emulsion material (with X-ray sensitive grains of the emulsion). However, both these parameters lead to deterioration of the linear resolution of the photographic material. Therefore, some optimum must be sought. The most suitable for this purpose are photographic materials developed for nuclear research, for example, Ilford L4 photographic plates [58, 59]. For this kind of emulsion, the size of

the undeveloped grain is about 0.1 μm at an emulsion-layer thickness of 20–50 μm. However, the light-exposed grains can swell up to 20 μm when developed. On the other hand, a significant thickness of the photographic layer also decreases the resolution because of optical parallax. Under optimal experimental conditions, the linear resolution of such emulsions can reach 2–10 μm.

In Russia, nuclear photographic plates with emulsions MR or MK with a layer thickness of 10–20 μm and a resolution of 250 and 500 line/mm, respectively, have been used to record X-ray topograms (Moscow Factory of Technical Photographic Plates).

Methods for the analysis of diffraction images of defects and obtaining information on the real structure of crystals are described in detail in reviews and monographs [43, 58, 59]. At the first stage, the topograms are usually obtained by reflection from several crystallographic planes $(h_1k_1l_1)$, $(h_2k_2l_2)$, $(h_3k_3l_3)$, ...; it is determined, in which reflections the extinction of the image of the observed defect occurs; and the spatial arrangement of defects in the crystal is found. This allows one to implement the type of elastic field associated with the defect. The next stage of analysis is numerical simulation of the diffraction image of the defect by using methods for solving the Takagi–Taupin equations [72, 73] and comparing the obtained models with the experiment. Unfortunately, the inverse problem, i.e., the problem of determining the defect type from the type of its diffraction image, is not always solved in a simple way. Therefore, such problems in difficult cases are unavoidably solved by the method of trial and error, i.e., the local field model is selected, and then the image is calculated and compared with the experimentally observed image [43, 44, 21].

The problem of determining the misalignment of blocks in crystal space is solved much more simply. In this case, it is necessary to measure the widths of the boundaries between grains (light and dark boundaries) of the crystal lattice (Fig. 5) and to determine the misalignment from the known parameters of the geometry of the experiment [58, 59, 74].

Summarizing the entire period of the development of X-ray topography since 1936, it can be stated that the future of X-ray topography is associated with the creation of new equipment, the development of new powerful laboratory microfocus radiation sources, new X-ray optical schemes, and the development of new quantitative methods for analyzing diffraction images, such as:

(i) studying the surface structure and defects on the surface of crystals;

(ii) development of new 2D X-ray detectors with a resolution of 1–5 μm;

(iii) development of new X-ray optical schemes using quasi-planar waves;

(iv) application of modern powerful X-ray radiation sources;

(v) acquiring information about the spatial position of the defect in the volume of the crystal (X-ray tomography based on laboratory sources, these studies are just beginning [75]);

(vi) development of new methods for controlling X-ray goniometers on the basis of acoustooptics, which provides rapid rearrangement of the X-ray optical scheme [63, 64].

Implementation of these areas brings X-ray topography to a new level. Analysis of the fine structure of the diffraction image allows one to determine the shape of the elastic deformation field formed by the crystal-lattice defect, to record and study very weak local microdeformations corresponding to crystal-lattice misalignments of about 10^{-2}–10^{-3} arc seconds at a very short exposure times of a few seconds [76]. The use of X-ray acoustooptic methods to control the X-ray experiment, powerful X-ray sources, and new detectors open up the possibility of studying the crystal structure in real time. X-ray topography methods, along with electron microscopy and atomic force microscopy, have become the key methods for studying the real structure of crystals in modern materials science.

CONCLUSIONS

Almost 80 years since the first publications, X-ray topography has followed a long, interesting track from the simplest Bragg schemes to modern multicrystal X-ray optical schemes, from the qualitative observation of crystal structure defects to extremely sensitive quantitative methods of measuring very weak local deformations generated by defects. X-ray topography played a decisive role in studying the real structure of semiconductor materials and developing methods for growing materials used in modern microelectronics. X-ray topography methods have become an important tool for scientific research in materials science, crystallography, and electronics.

Analysis of the mechanisms of X-ray contrast formation shows that the spatial resolution of X-ray topography methods is around 2–5 μm [21, 44]. This is a fairly modest resolution compared, for example, to electron microscopy. However, comparing the spatial resolution of X-ray topography methods with a resolution that can be achieved in methods of modern electron or atomic force microscopy (about 1 Å), it should always be borne in mind that the operating field can be about 10 cm^2 in X-ray topography methods and around 0.01–0.001 μm^2 in electron or atomic force microscopy [21, 74, 77]. Samples for electron microscopy must be specially prepared, namely, it is necessary to preliminarily obtain a thin foil of 0.1–0.01 μm in thickness, i.e., to practically destroy the test sample. When preparing a sample for X-ray topography, it is

sufficient to chemically polish the crystal surfaces to remove a thin surface layer (10–15 μm) that was damaged during mechanical processing of the sample. Neither the sample thickness nor its dimensions are of particular importance.

Indeed, these methods should not be viewed as competing with each other; they complement each other's capabilities. It should be added that X-ray topography has an extremely high sensitivity to local deformations of the crystal lattice. Modern multicrystal X-ray optical schemes allow one to sense and measure the contributions of local misalignments and dilatations. Changes in the local lattice turns and interplanar spacing correspond, in terms of the turn angles (according to the Wulff–Bragg ratio), to hundredths and even thousandths of arc seconds. Translating into a visual language, modern methods of X-ray topography enable the detection and measurement of the magnitude of the "local combined lattice distortion" in local regions of the crystal with dimensions of about 10 μm, which corresponds to the bending of planes to several hundred micrometers. The above reasoning allows us to state that X-ray topography methods, along with electron, tunneling, and atomic force microscopy, are the main methods for studying the real structure of crystals in modern materials science.

REFERENCES

1. A. Guinier, *Theorie et technique de la radiocristallographie* (Dunod, Paris, 1956).
2. Ya. S. Umanskii, *X-Ray Radiography of Metals* (Metallurgiya, Moscow, 1967) [in Russian].
3. V. I. Iveronova and G. P. Revkevich, *Theory of X-ray Scattering* (Moscow State Univ., Moscow, 1972) [in Russian].
4. W. Berg, Naturwissenschaften **19**, 391 (1931).
5. W. Berg, Z. Kristallogr. **89** (3), 286 (1934).
6. K. Kohra, J. Phys. Soc. Jpn. **17**, 589 (1962).
7. C. S. Barrett, Trans. AIME **161**, 15 (1945).
8. L. G. Schulz, Trans. AIME **200**, 1082 (1954).
9. T. Fujiwara, Mem. Def. Acad., Math., Phys., Chem. Eng. (Yokosuka, Jpn.) **2** (5), 127 (1963).
10. T. Fujiwara, S. Dohi, and T. Takeda, Mem. Def. Acad., Math., Phys., Chem. Eng. (Yokosuka, Jpn.) **3** (2), 17 (1963).
11. A. P. Turner, T. Vreeland, and D. P. Pope, Acta Crystallogr., Sect. A: Cryst. Phys., Diffr., Theor. Gen. Crystallogr. **24** (4), 452 (1968).
12. U. Bonse, Z. Phys. **153** (2), 278 (1958).
13. K. Kohra and S. Kikuta, Acta Crystallogr., Sect. A: Cryst. Phys., Diffr., Theor. Gen. Crystallogr. **24**, 200 (1968).
14. G. Borrmann, Z. Phys. **42**, 157 (1941).
15. A. R. Lang, Acta Crystallogr. **12**, 249 (1959).
16. V. M. Gundyrev, N. V. Belova, and V. O. Esin, USSR Inventor's Certificate No. 300817, Byull. Izobret., No. 13 (1971).
17. I. M. Shmyt'ko, V. Sh. Shekhtman, Yu. A. Ossipyan, and N. S. Afonikova, Ferroelectrics **96**, 151 (1989).
18. Yu. A. Osip'yan, V. Sh. Shekhtman, and I. M. Shmyt'ko, Pis'ma Zh. Eksp. Teor. Fiz. **47** (10), 501 (1988).
19. N. S. Afonikova, V. V. Borovkov, and I. M. Shmyt'ko, Fiz. Tverd. Tela **29** (3), 813 (1987).
20. N. S. Afonikova, V. Sh. Shekhtman, and I. M. Shmyt'ko, Fiz. Tverd. Tela **27** (11), 3201 (1985).
21. E. V. Suvorov and I. A. Smirnova, Usp. Fiz. Nauk **185** (9), 897 (2015).
22. V. M. Kaganer, N. O. Krylova, V. L. Indenbom, and I. L. Shul'pina, Fiz. Tverd. Tela **28** (8), 2343 (1986).
23. I. L. Shulpina, J. Appl. Phys. A **26** (4), 82 (1993).
24. E. V. Suvorov and I. L. Shul'pina, Poverkhnost, No. 7, 3 (2001).
25. I. A. Prokhorov, I. L. Shulpina, V. I. Strelov, et al., Phys. Status Solidi A **6**, 1902 (2005).
26. I. L. Shulpina and E. V. Suvorov, Bull. Russ. Acad. Sci.: Phys. **74** (11), 1488 (2010).
27. I. L. Shul'pina, S. S. Rouvimov, and R. N. Kyutt, J. Surf. Invest.: X-ray, Synchrotron Neutron Tech. **4** (1), 32 (2010).
28. I. L. Shul'pina, V. V. Ratnikov, V. A. Kozlov, et al., Tech. Phys. **59** (10), 1566 (2014).
29. L. I. Datsenko, V. B. Molodkin, and M. E. Osinovskii, *Dynamic X-ray Scattering by means of Real Crystals* (Naukova Dumka, Kiev, 1988) [in Russian].
30. L. N. Danil'chuk and T. A. Smorodina, Fiz. Tverd. Tela **7** (4), 1245 (1965).
31. L. N. Danil'chuk and V. I. Nikitenko, Fiz. Tverd. Tela **9** (7), 2027 (1967).
32. L. N. Danil'chuk, Fiz. Tverd. Tela **11**, 3085 (1969).
33. L. N. Danil'chuk, Vestn. Novgorod. Gos. Univ., No. 1, 12 (1995).
34. A. N. Builov and L. N. Danil'chuk, Tech. Phys. Lett. **28** (9), 762 (2002).
35. K. Kohra, M. Ando, and T. Matsushita, Nucl. Instrum. Methods **152**, 161 (1978).
36. A. Authier and A. R. Lang, J. Appl. Phys. **35**, 1956 (1964).
37. Y. Epelboin and A. Authier, Acta Crystallogr., Sect. A: Found. Crystallogr. **39**, 767 (1983).
38. E. V. Suvorov, V. I. Polovinkina, V. I. Nikitenko, and V. L. Indenbom, Phys. Status Solidi **26** (1), 385 (1974).
39. M. Yoshmatsu, *X-Ray Diffraction Micrography, The Lang Method* (Rigacu Denki, Tokyo, 1964).
40. S. Sh. Gendelev, L. M. Dedukh, V. I. Nikitenko, et al., Izv. Akad. Nauk SSSR, Ser. Fiz. **35** (6), 1210 (1971).
41. N. Kato, J. Phys. Soc. Jpn. **19** (1), 67 (1964).
42. N. Kato, J. Phys. Soc. Jpn. **19** (6), 971 (1964).
43. A. Authier, *Dynamical Theory of X-Ray Diffraction* (Science Publ., Oxford, 2001).
44. V. L. Indenbom and F. N. Chukhovskii, Usp. Fiz. Nauk **107** (2), 229 (1972).
45. V. L. Indenbom and F. N. Chukhovskii, Kristallografiya **16** (6), 1101 (1971).
46. V. G. Kohn, Crystallogr. Rep. **52** (4), 598 (2007).
47. Y. Ando, J. R. Patel, and N. Kato, J. Appl. Phys. **44** (10), 4405 (1973).

48. V. L. Indenbom, V. I. Nikitenko, E. V. Suvorov, and V. M. Kaganer, Phys. Status Solidi A **46** (1), 379 (1978).
49. I. L. Shul'pina, Zavod. Lab., Diagn. Mater. **66** (2), 25 (2000).
50. M. G. Mil'vidskii, Yu. A. Osip'yan, I. A. Smirnova, et al., Poverkhnost, No. **6**, 11 (2001).
51. I. L. Shul'pina, Zavod. Lab., Diagn. Mater. **73** (5), 30 (2007).
52. E. Rouv and J. Uiver, Usp. Fiz. Nauk **126** (2), 269 (1978).
53. I. M. Ternov, Usp. Fiz. Nauk **165** (4), 429 (1995).
54. H. Winick, J. Synchrotron Radiat. **5**, 168 (1998).
55. G. V. Fetisov, *Synchrotron Emission. Methods for Researching Matter Structure* (Fizmatlit, Moscow, 2007) [in Russian].
56. *Synchrotron Light Sources and Free-Electron Lasers. Accelerator Physics, Instrumentation and Science Applications,* Ed. by E. J. Jaeschke, (Springer, 2016).
57. T. Tuomi, K. Naukkarinen, and P. Rabe, Phys. Status Solidi A **25** (1), 93 (1974).
58. B. K. Tanner and M. A. Phil, *X-Ray Diffraction Topography* (Pergamon Press, New York, 1966).
59. D. K. Bowen and B. K. Tanner, *High Resolution X-ray Diffractometry and Topography* (Taylor & Francis, London, 1998).
60. J. Baruchel and J. Hartwig, J. Synchrotron Radiat. **9**, 107 (2002).
61. A. Zarka, B. Capelle, J. Detaint, and J. Schwartzel, J. Appl. Crystallogr. **21**, 967 (1988).
62. A. E. Voloshin, Doctoral Dissertation in Mathematics and Physics (A. V. Shubnikov Institute of Crystallography Russ. Acad. Sci., Moscow, 2013).
63. A. E. Blagov, P. A. Prosekov, A. V. Targonskii, and Ya. A. Eliovich, Crystallogr. Rep. **60** (2), 167 (2015).
64. A. E. Blagov, Yu. V. Pisarevskii, and M. V. Koval'chuk, Crystallogr. Rep. **61** (2), 170 (2016).
65. A. R. Lang and K. Reifsnide, Appl. Phys. Lett. **15** (8), 162 (1969).
66. J. Chikawa and I. Fujmoto, Appl. Phys. Lett. **13** (11), 18 (1968).
67. E. V. Suvorov, Elektron. Prom-st. **6**, 49 (1979).
68. A. Koch, C. Raven, P. Spanne, and A. Snigirev, J. Opt. Soc. Am. A **15**, 1940 (1998).
69. Y. Amemiya, J. Synchrotron Radiat. **2**, 13 (1995).
70. S. M. Grunera, W. Mark, and E. F. Eikenberry, Rev. Sci. Instrum. **73** (8), 121 (2002).
71. R. C. Harrison, Nucl. Instrum. Methods Phys. Res., Sect. A **347**, 529 (1994).
72. S. Takagi, Acta Crystallogr. **15**, 1311 (1962).
73. D. Taupen, Bull. Soc. Fr. Mineral. Cristallogr. **87**, 469 (1964).
74. E. V. Suvorov, *Methods for Researching Real Structure and Composition of Materials* (National Univ. of Science and Technology MISiS, Moscow, 2011) [in Russian].
75. V. E. Prun, A. V. Buzmakov, M. V. Chukalina, et al., Autom. Remote Control (Engl. Transl.) **74** (10), 1670 (2013).
76. E. V. Suvorov and I. A. Smirnova, Tech. Phys. Lett. **42** (9), 955 (2016).
77. J. C. H. Spense, *Experimental High-Resolution Electron Microscopy* (Claredon Press, Oxford, 1981).

Translated by O. Kadkin